Melting of math xmlns="http://www.w3.org/1998/Math/MathML">mrow>mi >MgSi/mi>msub>mi mathvariant="normal">O/mi> mn>3/mn>/msub>/mrow>/math> determined by machine learning potentials

Jie Deng, Haiyang Niu, Junwei Hu, Mingyi Chen, and Lars Stixrude

Phys. Rev. B **107**, 064103 — Published 13 February 2023

DOI: 10.1103/PhysRevB.107.064103

Melting of $MgSiO_3$ determined by machine learning potentials

Authors: Jie Deng[a,b]*, Haiyang Niu[c]*, Junwei Hu[c], Mingyi Chen[c], and Lars Stixrude[a]

Affiliation:

[a] Department of Earth, Planetary, and Space Sciences, University of California, Los Angeles, CA

[b] Department of Geosciences, Princeton University, Princeton, NJ

[c] State Key Laboratory of Solidification Processing, International Center for Materials Discovery, School of Materials Science and Engineering, Northwestern Polytechnical University, Xi'an 710072, P.R. China.

* corresponding authors: jie.deng@princeton.edu; haiyang.niu@nwpu.edu.cn

Keywords:

Melting, $MgSiO_3$, Machine learning

Abstract

Melting in the deep rocky portions of planets is important for understanding the thermal evolution of these bodies and the possible generation of magnetic fields in their underlying metallic cores. But the melting temperature of silicates is poorly constrained at the pressures expected in super-Earth exoplanets, the most abundant type of planets in the galaxy. Here, we propose an iterative learning scheme that combines enhanced sampling, feature selection, and deep learning, and develop a unified machine learning potential of *ab initio* quality valid over a wide pressure-temperature range to determine the melting temperature of $MgSiO_3$. The melting temperature of the high-pressure, post-perovskite phase, important for super-Earths, increases more rapidly with increasing pressure than that of the lower pressure perovskite phase, stable at the base of Earth's mantle. The volume of the liquid closely approaches that of the solid phases at the highest pressure of our study. Our computed triple point constrains the Clapeyron slope of the perovskite to post-perovskite transition, which we compare with observations of seismic reflectivity at the base of Earth's mantle to calibrate Earth's core heat flux.

I. INTRODUCTION

Cosmic abundances, stellar spectroscopy, observations of polluted white dwarfs, and mass-radius relations point towards the abundance of planets in our galaxy with Earth-like compositions, with a mantle dominated by the $MgSiO_3$ component (~70% in the case of Earth) and an iron-rich core, and masses similar to or greater than that of Earth (1-10 Earth masses) [1,2]. Studies of planetary accretion and thermal evolution suggest that these bodies may have begun in a completely molten state and that mantle and core are still partially molten after billions of years [3-6]. The melting temperature of $MgSiO_3$ exerts a first-order control on thermal evolution because of the large change in viscosity across the melting transition, which sets the time scale for thermal evolution. The density contrast between liquid and solid is also important because this determines whether crystals freezing out of a deep molten portion of a planet sink or float, setting the vector of chemical evolution [7].

The melting temperature of $MgSiO_3$ has therefore attracted considerable attention, yet no consensus exists, in part because of the experimental challenges at very high pressure [8-11]. While melting of the bridgmanite phase has received the most attention, melting of its high-pressure polymorph – post-perovskite – is also important because this is the stable crystalline phase at pressures greater than 140 GPa (nearly coinciding with the pressure at the base of Earth's mantle) to pressures as high as 750 GPa [12] (the pressure at the base of the mantle in a 5 mass super-Earth). The melting temperature also constrains the triple point at which all three phases are stable (bridgmanite, post-perovskite, liquid) and therefore the Clapeyron slope of the solid-solid transition, which is observed via seismic reflection at the base of Earth's mantle [13]. The Clapeyron slope of the solid-solid transition is also very uncertain at present, leading to large uncertainties in the heat flux from Earth's core [14], the existence of an active dynamo to generate the magnetic field, and the habitability of planets.

Simulation of the $MgSiO_3$ system at deep Earth and super-Earth conditions presents many challenges. Among these are the subtle energetics of structurally similar phases and the nature of the bonding, which is dominantly ionic, but may also include covalent and metallic contributions, which may account for the discrepancy of previous attempts to simulate melting in this system on the basis of empirical potentials [15-17]. The situation points towards density functional theory (DFT) as an accurate means of representing the energetics of this system that makes no *a priori* assumption about the nature of bonding. However, DFT is very costly, and melting is a rare event in standard molecular dynamics simulations, which is why there have been no *ab initio* determinations of the melting temperature. The solid-liquid two-phase coexistence simulation has been shown to yield robust results for many simpler materials [18-20]. However, the two-phase method requires a large system size to stabilize the coexistence, and very long runs, thus rendering this method computationally demanding or even impossible in the context of the density functional theory.

Machine learning potentials (MLPs) are an emerging approach to atomistic simulations that combines, in principle, *ab initio* accuracy, with the ability to simulate large systems for a very long

time [21,22]. Therefore, MLPs are well suited to perform two-phase coexistence simulation and study melting behavior. However, developing a robust MLP of a three-component system of multiple phases over a wide range of pressure and temperature is very challenging [23] and has not yet been attempted. Machine learning potentials are generally trained on DFT results for a finite set of configurations, for example from an *ab initio* molecular dynamics simulation, but there are three difficulties. First, the range of thermodynamic conditions sampled by a molecular dynamics simulation is narrow, necessitating multiple simulations covering the pressure-temperature range of interest. Second, in any one of these simulations, only one phase will be sampled, since phase transitions are rare events, biasing the MLP towards that phase. Third, transitions states, crucial for capturing the physics of the solid-liquid interface are transient and therefore rarely encountered.

We have overcome these challenges by combining enhanced sampling of configuration space [24] with the deep learning algorithm [22]. The enhanced sampling is driven by a carefully designed set of collective variables (CVs) to capture configurations corresponding to multiple phases, two-phase interfaces, and rare transition states. These methods have previously been used to study phase transitions in simpler systems over much narrower ranges of pressure and temperature [23,25]. We develop a unified machine learning potential that encompasses the physics of the three phases of interest over a wide range of pressure and temperature.

II. BUILDING THE MACHINE LEARNING POTENTIAL

A machine learning potential is a non-parametric representation that approximates the Born-Oppenheimer potential energy surface to arbitrary accuracy. In our approach, the machine learning potential is trained on a set of configurations drawn from multithermal and multibaric (MTMP) simulations [24], which are used to efficiently sample multi-phase configuration space. The key to driving the sampling is the design of an appropriate collective variable (CV) that captures key aspects of the structure. We use an iterative learning scheme to efficiently select distinct samples from the molecular dynamics trajectories. We have found that efficient training of the machine learning potential is greatly facilitated by performing the underlying ab initio calculations at very high precision.

A. Multithermal–multibaric simulation

The multithermal and multibaric simulation is an enhanced sampling technique designed to sample uniformly in energy and volume simultaneously by taking the intervals of temperature and pressure as inputs. It is based on variationally enhanced sampling, where a functional of the bias potential $V(\mathbf{s})$ is introduced as

$$\Omega[V(\mathbf{s})] = \frac{1}{\beta}\log\frac{\int d\boldsymbol{s} e^{-\beta[F(\mathbf{s})+V(\mathbf{s})]}}{\int d\boldsymbol{s} e^{-\beta F(\mathbf{s})}} + \int d\boldsymbol{s} p(\mathbf{s}) V(\mathbf{s}) \quad (1)$$

where $\mathbf{s}$ is a set of collective variables (CV) that are a function of the atomic coordinates $\mathbf{R}$; $\beta = 1/k_B T$ is the inverse temperature with k_B and T the Boltzmann constant and temperature, respectively; $F(\mathbf{s})$ is Helmholtz free energy with $F(\mathbf{s}) = -1/\beta \log \int \delta[\mathbf{s} - \mathbf{s}(\mathbf{R})] d\mathbf{R} e^{-\beta U(\mathbf{R})}$

where $U(\mathbf{R})$ is the interatomic potential; and $p(\mathbf{s})$ is a preassigned target distribution. This functional $\Omega[V(\mathbf{s})]$ is guaranteed to be convex and has a stationary point at

$$V(\mathbf{s}) = -\frac{\ln p(\mathbf{s})}{\beta} - F(\mathbf{s}) \qquad (2)$$

In this way, one transforms the problem of modifying the Hamiltonian to an optimization problem given the target distribution $p(\mathbf{s})$. To generate a multithermal–multibaric ensemble at the pressure and temperature intervals of $P_1<P<P_2$ and $\beta_1 > \beta > \beta_2$, respectively, one chooses the potential energy $E = U(\mathbf{R})$ and the volume V as CVs to perform a variationally enhanced sampling simulation with the following target distribution

$$p(E,V) = \begin{cases} \frac{1}{\Omega_{E,V}}, & \text{if there is at least one } \beta \text{ and } P \text{ such that } \beta F_{\beta,P(E,V)} < \varepsilon \\ 0, & \text{otherwise} \end{cases}, \qquad (3)$$

where ϵ/β is a predefined energy threshold. The value of ϵ/β is set according to the nucleation/melting energy barrier between the solid and liquid states. In practice, we have performed VES simulation using s_x as CV to roughly estimate the energy barrier, and ϵ/β should be larger than the energy barrier.

We used PLUMED 2 [26] with variationally enhanced sampling module and LAMMPS [27,28] to perform the multithermal–multibaric simulation on systems of $MgSiO_3$ consisting of 160 atoms. The bias potential was constructed using variationally enhanced sampling with the energy E, the volume V and s_x (Eq. 4) as CVs. The basis sets of the bias potential are Legendre polynomials of order 8 for each CV. As a result, there are 729 variational coefficients to be optimized. The integrals of the target distribution were performed on a grid of size 40 × 40 × 40. Multiple MTMP runs with a pressure interval of 20 GPa are performed. For instance, in the temperature range of 3500 to 5000 K and pressure range of 40 to 60 GPa, the intervals where the polynomials were defined are $-108000 < E < -9500$ kJ/mol, $1120 < V < 1480$ Å^3, $-200 < s_x < 3000$, and the exploration threshold ϵ/β is set to 150 k_BT. To improve computing performance, the target distribution was discretized on a grid of dimensions 40×40×40 and smoothed using Gaussians with $\sigma_E = 200$ kJ/mol, $\sigma_V = 0.05$ nm^3, and $\sigma_{sx} = 2$. The coefficients of the bias potential were optimized every 500 steps using the averaged stochastic gradient descent algorithm with a step size of $\mu = 10$ kJ/mol.

B. Collective variables

For the collective variable (CV), we use the structure factor, which was shown to be an effective CV to drive the first-order phase transition in simpler systems [29]. In our more complex system, we found it essential that the CV contain information from partial structure factors at multiple scattering vectors in order to effectively differentiate bridgmanite, post-perovskite, and liquid as summarized in Fig. 1.

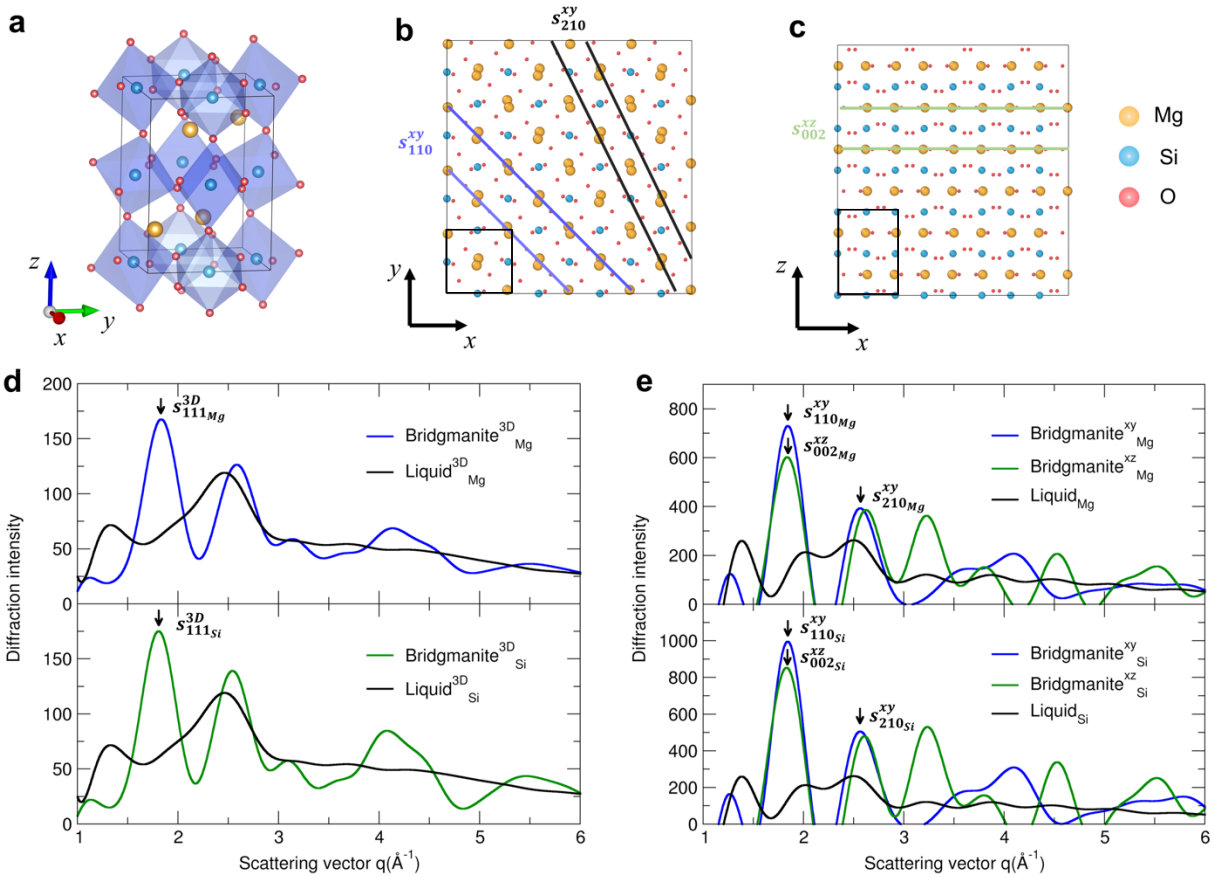

Figure 1. Simulated structure factors (i.e., diffraction intensity) of bridgmanite (a) and liquid. (**a**) Schematic illustration of the crystal structure of bridgmanite, where the orthorhombic unit-cell is indicated by solid box. **(b-c)** Projected crystal structures of bridgmanite in the *x*-*y* and *x*-*z* planes, respectively. **(d)** and **(e)** display the simulated structure factors of bridgmanite and liquid from the three-dimensional and two-dimensional perspectives, respectively. The components of the collective variable, in which the descriptors, components of the collective variable s_x, is highlighted with black arrows. The corresponding planes of the two-dimensional descriptors are denoted in (b-c). The subscript *i* (e.g., Mg, Si) indicates that only element *i* is taken into accounts in the calculations.

The collective variable s_x to drive the phase transition between bridgmanite and liquid is a linear combination of seven descriptors as

$$s_x = s^{3D}_{111_{Mg}} + s^{3D}_{111_{Si}} + s^{xy}_{110_{Mg}} + s^{xy}_{210_{Mg}} + s^{xz}_{002_{Mg}} + s^{xy}_{110_{Si}} + s^{xy}_{210_{Si}} + s^{xz}_{002_{Si}}, \quad (4)$$

in which the Debye form of structure factor is employed to calculate each component, i.e., s^{3D}_{hkl}, s^{xy}_{hkl}, and s^{xz}_{hkl} are defined below. Due to the complexity of the system, the contribution of Mg and Si atoms from the three-dimensional (3D) and two-dimensional (2D) in the *x*-*y* and *x*-*z* planes are counted separately (Fig. 1) following [30]. The CV to drive the phase transition between post-perovskite and liquid is constructed following the same procedure. For simplicity, s_x is rescaled to the range of 0 to 1, in which 1 refers to perfect solid state and 0 refers to disordered state with lowest structure factor intensities.

The first two descriptors correspond to the first main peak intensities of the structure factors of Mg and Si atoms, respectively, and are calculated with the Debye scattering function:

$$s_{hkl}^{3D} = \frac{1}{N}\sum_{i=1}^{N}\sum_{i=1}^{N} f_i(q) f_j(q) \frac{\sin(Q \cdot R_{ij})}{Q \cdot R_{ij}} w(R_{ij}), \tag{5}$$

in which q is the scattering vector, hkl refers to the Miller index of bridgmanite, $f_i(q)$ and $f_j(q)$ are the atomic scattering form factors and R_{ij} is the distance between atoms i and j. A window function $w(R_{ij}) = \frac{\sin(Q \cdot R_{ij}/R_c)}{Q \cdot R_{ij}/R_c}$ is used to get a smooth behavior of the structure factor; R_c (=16 Å) refers to upper limit distance.

The descriptors $s_{110_{Mg}}^{xy}$, $s_{210_{Mg}}^{xy}$, $s_{110_{Si}}^{xy}$, $s_{210_{Si}}^{xy}$ correspond to the intensities of the two main peaks of the structure factor of one slice layer which is projected into the *x-y* plane, which are given by:

$$s_{hkl}^{xy} = \frac{1}{N}\sum_{i=1}^{N}\sum_{i=1}^{N} f_i(q) f_j(q) J_0(Q \cdot R_{ij}^{xy})\, w^{xy}(R_{ij}^{xy}) w^{z}(R_{ij}^{z}), \tag{6}$$

in which J_0 is the 0th order of the first kind Bessel function, R_{ij}^{xy} is the distance between atoms i and j in the *x-y* plane; $w^{xy}(R_{ij}^{xy}) = \frac{1}{1+e^{\sigma(R_{ij}^{xy} - R_c^{xy})}}$ refers to a switching function; and R_c^{xy} (=10 Å) is the distance cutoff,. In addition, only atoms within a distance cutoff R_c^z (=3.5 Å) along the z direction are taken into account, and $w^z(R_{ij}^z) = \frac{1}{1+e^{\sigma(R_{ij}^z - R_c^z)}}$ refers to a switching function to make the descriptor smooth.

Similarly, descriptors s_{Mg}^{xz} and s_{Si}^{xz} are calculated as:

$$s_{hkl}^{xz} = \frac{1}{N}\sum_{i=1}^{N}\sum_{i=1}^{N} f_i(q) f_j(q) J_0(Q \cdot R_{ij}^{xz})\, w^{xz}(R_{ij}^{xz}) w^{y}(R_{ij}^{y}), \tag{7}$$

where R_c^{xz} and R_c^{y} are set to 10 and 5.2 Å, respectively.

In order to validate the sampling effectiveness of such CV (Eq. 4), we have further analyzed the local atomic environment of the configurations with a short-range order parameter. Here we adopted an orientationally targeted order parameters[31] building on the smooth overlap of atomic positions (SOAP). The local environment around an atom is denoted as χ, and the associated local density is written as

$$\rho_\chi(\boldsymbol{r}) = \sum_{i \in \chi} e^{\frac{-|\boldsymbol{r}_i - \boldsymbol{r}|^2}{2\sigma^2}} \tag{8}$$

in which i runs over the neighbors in the environment χ, $\boldsymbol{r}_i$ are the coordinates of the neighboring atoms relative to the central atom, and $\sigma^2$is the variance of the Gaussian functions. Here we set σ to 0.5. In order to measure the difference between the environment χ and χ_0 of the reference structure that contains n reference positions, here the perfect crystal phase is used as the refence

structure. Importantly, the three element Mg, Si and O all have unique local environments. The similarity of two environments are compared by

$$k_{\chi_0}(\chi) = \int dr\, \rho_{\chi}(\boldsymbol{r})\rho_{\chi_0}(\boldsymbol{r}) \qquad (9)$$

A spherical average over all the possible orientations of the refence χ_0 is then performed to get the SOAP kernel. As the orientation of the refence χ_0 is fixed, the similarity can be trivially performed and normalized to

$$\tilde{k}_{\chi_0}(\chi) = \frac{k_{\chi_0}(\chi)}{k_{\chi_0}(\chi_0)} = \frac{1}{N}\sum_{i\in\chi}\sum_{j\in\chi_0} e^{\frac{-|\boldsymbol{r}_i-\boldsymbol{r}_j^0|^2}{4\sigma^2}} \qquad (10)$$

where N is the atom number in the configuration. Such CV is a per atom crystallinity metric of the specific phase considered.

C. Iterative learning scheme

Due to the vast pressure and temperature range targeted and the complex nature of $MgSiO_3$ system, we use an iterative training scheme to train and gradually refine the MLP (Fig. 2). Here, one iteration means training a new MLP with updated training set. After seven iterations, we find a sufficiently robust and unified MLP for $MgSiO_3$ bridgmanite, post-perovskite, and liquid at 0-220 GPa and 2000-8000 K. We emphasize that the feature selection with PCA and the iterative training is crucial to building a balanced and succinct training set. Indeed, the final training set only consists of 4324 configurations while covering three phases over 6000 K and 220 GPa, compared with typically tens of thousands of frames for mono-atomic species at very narrow pressure and temperature conditions [23,25]. Compared with other active learning algorithm like DP-GEN, the iterative learning scheme presents two improvements: 1) efficient enhanced sampling is embedded in the workflow; 2) we use PCA analysis and comparison between the MLP prediction and VASP results (ground truth) to select the candidate frames, while DP-GEN relies on the model deviation of the candidate frames only. We found that the model deviation, although being computationally more efficient, is prone to selecting frames that are already predicted very well by the MLP, especially when the threshold of the model deviation is not well set.

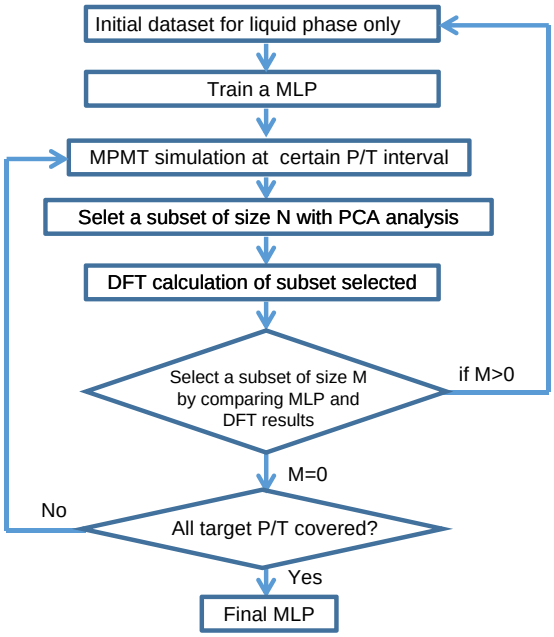

Figure 2. Flowchart of the iterative training scheme. 1) We first build an initial dataset for liquid phase only and train a preliminary MLP as reported in our recent study [32]. Liquid, as a disordered phase, may encompass some of the local environments of the solid phases, and thus may serve as a good starting point for generating a unified MLP for both solid and liquid phases. 2) Multithermal–multibaric (MTMP) simulations are performed with the MLP using LAMMPS interfaced with PLUMED 2. Here, PLUMED 2 is used to calculate the CVs and implement the enhanced sampling method. The target pressure and temperature ranges are very large in this study, making it difficult to cover in one multithermal–multibaric simulation. We find that MTMP simulations with ~20 GPa and ~2000 K intervals yield good convergence and can sample the phase transition sufficiently. As a result, the target P/T ranges are divided into 20 GPa and 2000 K bins along the melting curves of bridgmanite and post-perovskite [4,33]. We gradually update the P/T intervals with the iteration. 3) The resulting trajectories are saved every 500 timesteps. The saved frames are converted to design matrices based on the smooth overlap of atomic positions descriptor [34]. We then perform principal component analysis on these design matrices and select the candidate configurations using the farthest point sampling technique [35,36]. The size of candidate configurations N is large at first a few iterations and gradually decreases at later iterations. Specifically, N=1000-2000 for the first two iterations, N=50-100 for the rest of iterations. 4) The selected frames were recalculated with DFT. The resulting energies and forces, are compared with the MLP predicted ones. For the first three iterations, the configurations with both energy difference >15 meV/atom and atomic forces difference >0.5 eV/Å are selected. For the rest of iterations, we relax the selection criteria to energy difference >5 meV/atom and atomic forces difference >0.25 eV/Å. The size of the selected configurations in this step is M. We emphasize the selection criteria here is unlikely to be universal for all other systems but the principle that relaxing the selection criteria with iterations should apply. 5) The selected configurations will be combined with the initial dataset to train a new MLP. We re-iterate above steps until we cannot select frames in step (4) (i.e., M=0) and all the target pressures and temperatures are covered by MTMP simulations in step 2).

D. DeePMD approach.

The DeePMD approach adopts an end-to-end strategy [22,37] and does not make a priori assumptions about the form of the descriptor but rather uses a deep neural network to determine its form based only on the spatial location, in a suitably defined coordinate frame, of the neighboring atoms. Neural networks are widely used in the development of machine learning potentials because they are, in principle, capable of approximating any continuous function to arbitrary accuracy [32,38,39]. With DeePMD, one uses a neural network to find the functional form of the descriptor and a second neural network (fitting network) to determine the form of the potential energy surface. The fitting network is composed of three layers with 240 nodes in each layer. A cutoff of 6 Å is employed to describe the atomic local environments. The loss function is defined as

$$L(p_\epsilon, p_f, p_\xi) = p_\epsilon \Delta\epsilon^2 + \frac{p_f}{3N}\sum_i |\Delta \boldsymbol{F}_i| + \frac{p_\xi}{9}\|\Delta\xi\|^2, \qquad (11)$$

where p_ϵ, p_f, p_ξ are tunable prefactors for difference between the MLP prediction and training data. ϵ is the energy per atom; $\boldsymbol{F}_i$ atomic force of atom i ; ξ the virial tensor divided by N; N the numbrer of atoms. We adopt the conventional setting of increasing both p_ϵ and p_ξ from 0.02 to 1 while decreasing p_f from 1000 to 1 over the course of training.

E. *Ab initio* calculations

All *ab initio* calculations were performed on $MgSiO_3$ consisting of 160 atoms based on DFT in the PBEsol approximation [40] using VASP [41]. We used the projector augmented wave (PAW) method [42] as implemented in VASP [41]. We use the PBEsol approximation as it has been found to yield good agreement with experimental measurements of physical properties of silicates and oxides [43-45] and melting temperatures of MgO [46]. The core radii are O: 0.820 Å ($2s^2 2p^4$), Si: 1.312 Å ($3s^2 3p^2$), Mg: 1.058 Å ($2p^6 3s^2$). To construct the initial dataset, we perform *ab initio* molecular dynamics (AIMD) simulations with relatively low precision settings: energy cutoff of 500 eV, energy cutoff of 10^{-4} eV, and Gamma-point only k-mesh. AIMD simulations are performed in the NVT ensemble (constant number of atoms, volume, and temperature) using the Nosé-Hoover thermostat [47] and run for 5-20 ps with 1 fs time step. We assume thermal equilibrium between ions and electrons via the Mermin functional [48].

The configurations generated by these AIMD simulations as well as the multithermal and/or multibaric MD simulations were then selected to construct the MLP. The energy, force, and stress of these selected configurations were recalculated at much higher precision with: the energy cutoff that sets the size of the basis set increased from 500 eV to 800 eV, the precision to which the self-consistent solution to the Kohn-Sham equations is found lowered form 10^{-4} eV to 10^{-6} eV, and sampling of the Brillouin zone increased from the Gamma-point only to a 2×2×2 Monkhorst-Pack mesh. We found this high precision recalculation to be essential for optimizing the accuracy and scope of the MLP [32] (Fig. 3).

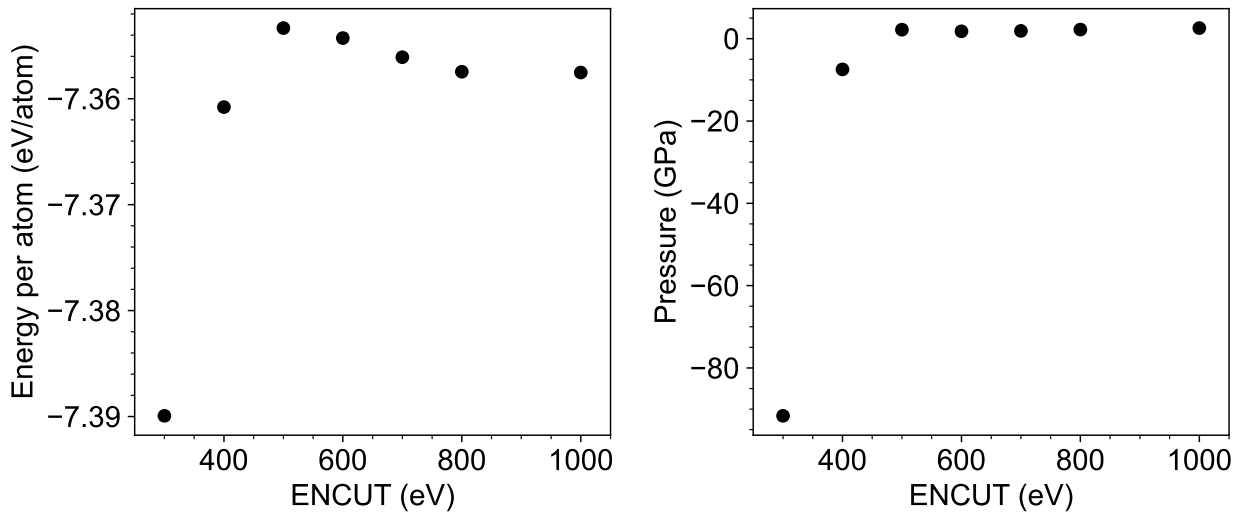

Figure 3. Convergence tests of total energy (a) and pressure (b) with varying energy cutoff (ENCUT flag in VASP) for 32 $MgSiO_3$ bridgmanite at static condition. An energy cutoff of 800 eV is sufficient to obtain converged results for both energy and pressure.

F. Simulations

For two-phase simulations, we use LAMMPS to build a 2-phase model of coexisting solid and liquid with the ratio of 1:1. Supercells of 900 atoms are constructed (3× 3 × 5 for *Pbnm* bridgmanite and 3 × 5 × 3 for *Cmcm* post-perovskite) and then relaxed for 1000 steps at the desired pressure and temperature conditions in the NPT ensemble. The relaxed cell is then used to perform NVT simulations at high temperatures far exceeding the melting temperatures with the atoms of half the cell fixed and the force applied to these atoms set to be 0. The resulting structure is half-molten and half-crystalline. We relaxed this structure again at the desired pressure and temperature conditions for 1000 steps to obtain the initial configuration for two-phase simulations. We also tested the size effect on the melting temperature by exploring larger system sizes of 1800 atoms and 3000 atoms, and found that systems of 900 atoms are sufficient to yield identical melting points as those larger systems.

Simulations on the two-phase cell were performed at the desired pressure and temperature conditions (NPT). If the whole cell is molten (crystallized) in the end, the simulation temperature is above (below) the melting point. The state of the system can be determined by interrogating the radial distribution functions. In this way, we can obtain the upper and lower bounds of the melting curve.

Phonon dispersions and zero-point energy were performed using the PHONOPY program [49]. Real-space force constants were calculated with density functional perturbation theory [50], with 2×2×2 and 4×1×2 supercells for bridgmanite and post-perovskite, respectively.

III. RESULTS

A. Sampling of Configuration Space

Our approach yields a broad sampling of configuration space and an efficient selection of representative configurations (Fig. 4). From a single MTMP run (40-60 GPa, 3000-5000 K), we generate liquid and bridgmanite configurations as well as configurations containing an interface between the two phases, and configurations containing distorted and defective crystalline structures. Post-processing with principal component analysis (PCA) selection and an iterative learning scheme yield balanced and succinct sampling over this range (Fig. 4). Indeed, the final training set is very small, consisting of only 4324 configurations, while covering a wide temperature and pressure (2000 to 8000 K and 0 GPa to 220 GPa), compared with typically tens of thousands of frames for mono-atomic species over much narrower ranges of pressure and temperature conditions [23,25].

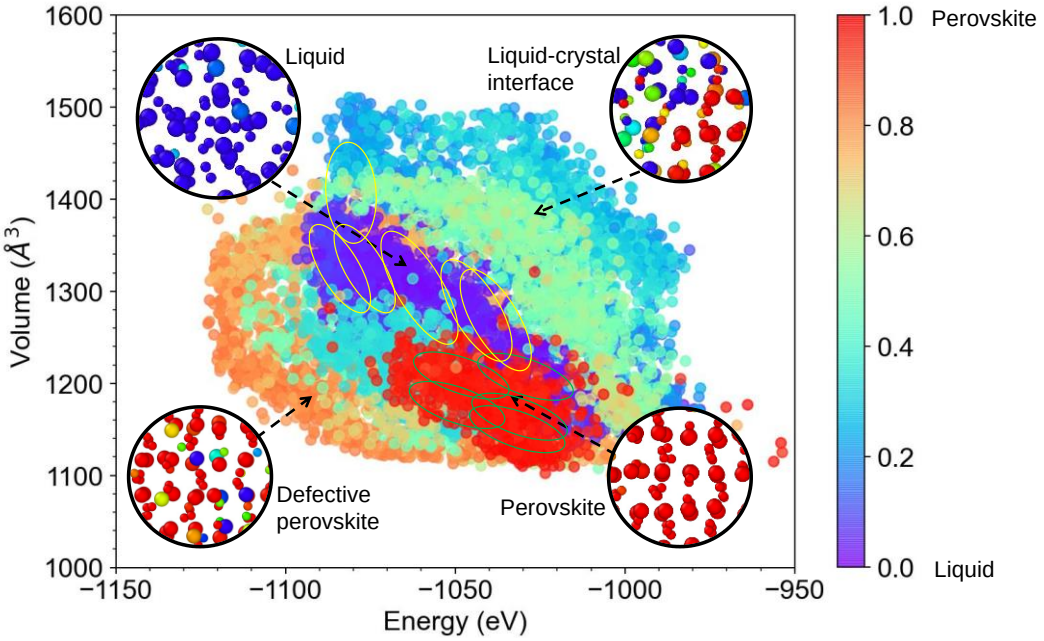

Figure 4. Configurations explored by multi-thermal multibaric simulations at 40-60 GPa and 3000-5000 K. The energy of the system (160 atoms) is plotted against volume and color-coded by the value of collective variable (CV) defined in Eq. 4. Large and small CVs indicate a perovskite-like or liquid-like state, respectively. Snapshots of configurations are shown in the circles with atoms color-coded based on the orientationally targeted order parameters [31] building on the smooth overlap of atomic positions (SOAP) [34], with red indicating perovskite-like and blue indicating liquid-like local atomic environments. The yellow and green ellipses show the regions sampled by standard molecular dynamics simulations at the same P/T range for liquid and solid states, respectively.

B. Benchmarks of the Machine Learning Potential

We compare the energies, atomic forces, and stresses from the machine learning potential with those from DFT simulations for 35585 configurations that are not included in the training set (Fig. 5). The root-mean-square errors of the energies, atomic forces, and stresses are 4.9 meV/atom, 0.24 eV/Å, and 0.37 GPa, respectively. These uncertainties are comparable to the typical precision of *ab initio* molecular dynamics simulations [45]. As all the testing structures supercells, the

robustness of the MLP in predicting properties larger systems is unclear. We performed another verification test with data obtained using a larger supercell with 320 atoms. This structure is not included in the training set. The RMSE of energy prediction is similar to the error in the testing sets (Fig. 6). This verification test further proved the accuracy of energy prediction and also demonstrated the transferability of the MLP to larger structures.

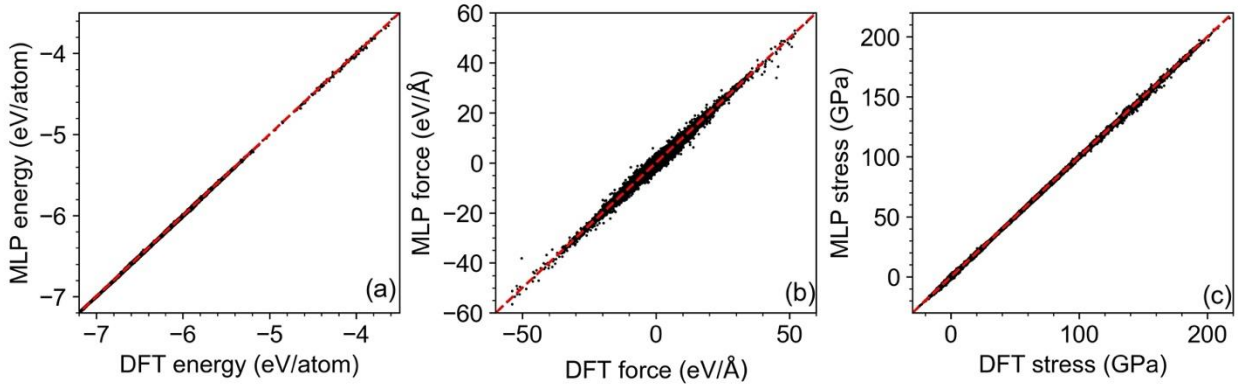

Figure 5. Comparisons of energies (a), atomic forces (b), and stresses (c) between DFT and the machine learning potential (MLP) for all the test data at 2000 to 8000 K and pressures from ~0 GPa to 220 GPa. 35585 energies, 17080800 force components, and 213510 stress components are included in these comparisons. The red dashed lines are guides for perfect matches.

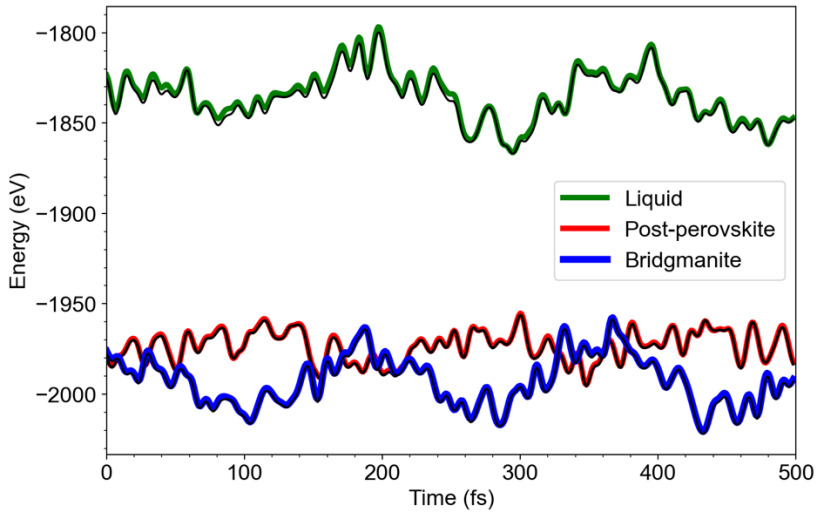

Figure 6. Comparisons of the total energy changes along molecular dynamics trajectories between the DFT (thick colored lines) and MLP potential (thin black lines) for $MgSiO_3$ bridgmanite (blue), post-perovskite (red), and liquid (green) at 140 GPa and 5000 K. The models used in this simulation contain 320 atoms, and none of the structures in the trajectories were included in the training set. The root mean square error of MLP is 4.2, 2.4, 7.1 meV/atom for perovskite, post-perovskite, and liquid, respectively.

C. Two-Phase Simulations

Two-phase simulations yield precise determinations of the melting temperature. Starting with a two-phase simulation cell of bridgmanite at 140 GPa, a simulation at 6100 K melts completely after 260 ps, whereas a simulation at 6000 K crystallizes after 730 ps (Fig. 7). Post-perovskite, on the hand, melts at 6000 K and crystalizes at 5900 K (Fig. 8). These simulations, performed at constant pressure and temperature show that the system expands upon melting, and contracts upon crystallization, yielding the volume of melting, the Clapeyron slope ($\Gamma = dP/dT_m$) and the entropy of melting ($\Delta S_m = \Gamma \Delta V_m$) (Table 1).

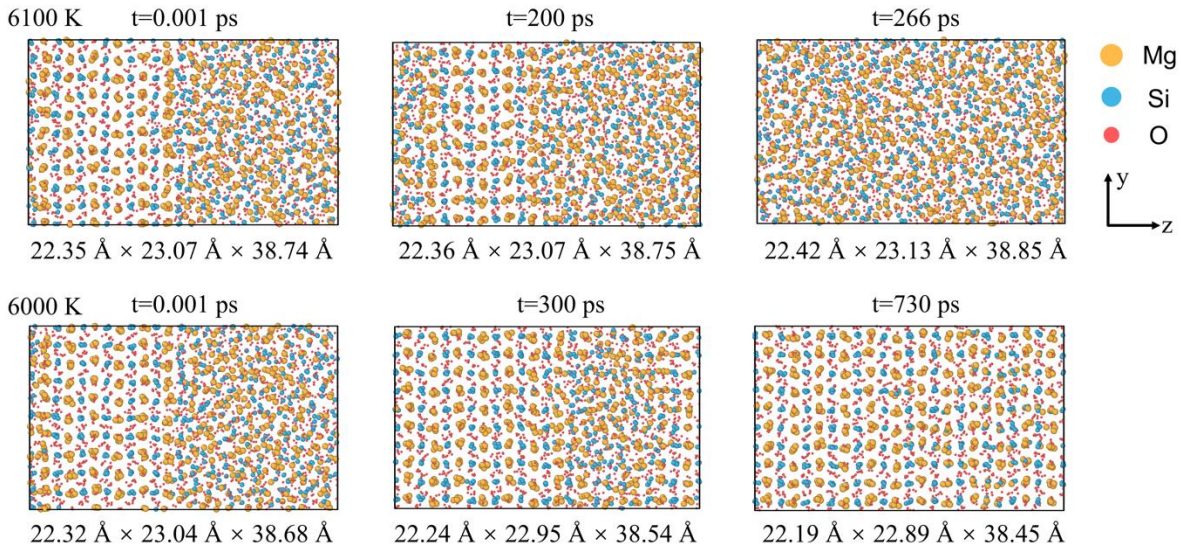

Figure 7. Machine learning molecular dynamics simulations of the coexistence of $MgSiO_3$ bridgmanite and liquid at 140 GPa and 6100 K (upper panel) and 6000 K (lower panel). The simulation cell contains 600 $MgSiO_3$ formula units (3000 atoms). The simulation timestep and the corresponding cell shape are also shown.

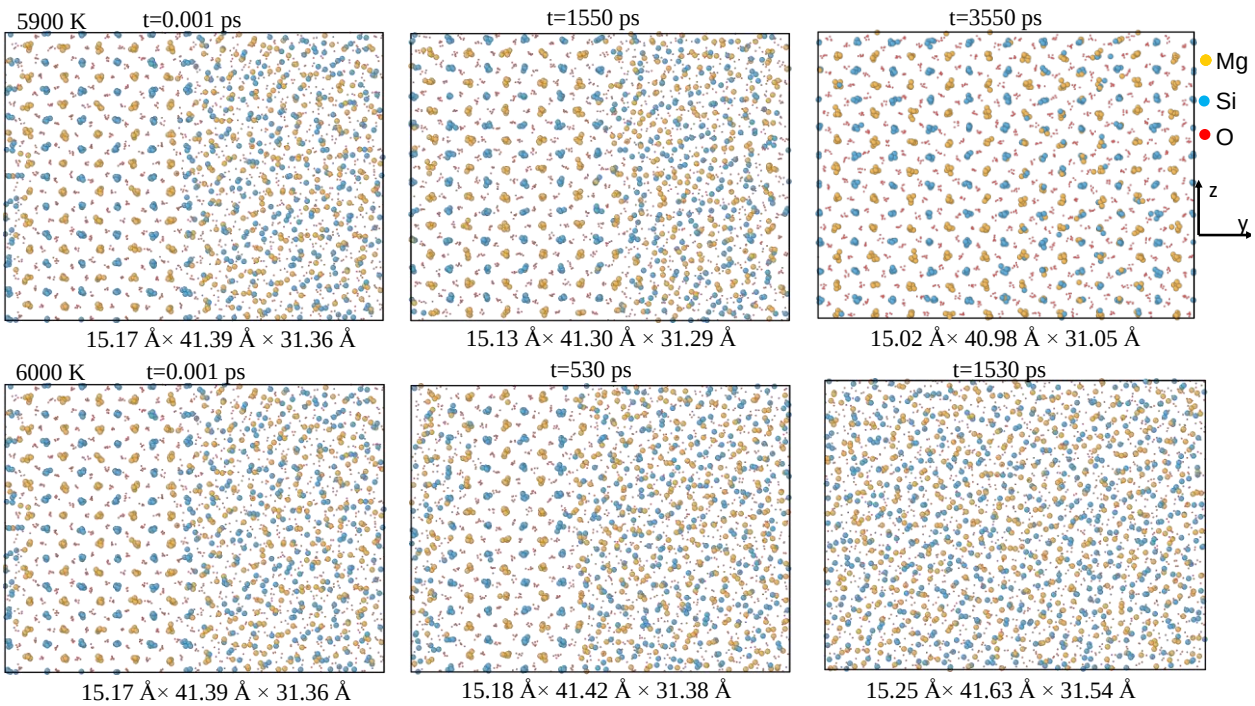

Figure 8. Machine learning molecular dynamics simulations of the coexistence of $MgSiO_3$ post-perovksite and liquid at 140 GPa and 5900 K (upper panel) and 6000 K (lower panel). The simulation cell contains 600 $MgSiO_3$ formula units (3000 atoms). The simulation timestep and the corresponding cell shape are also shown.

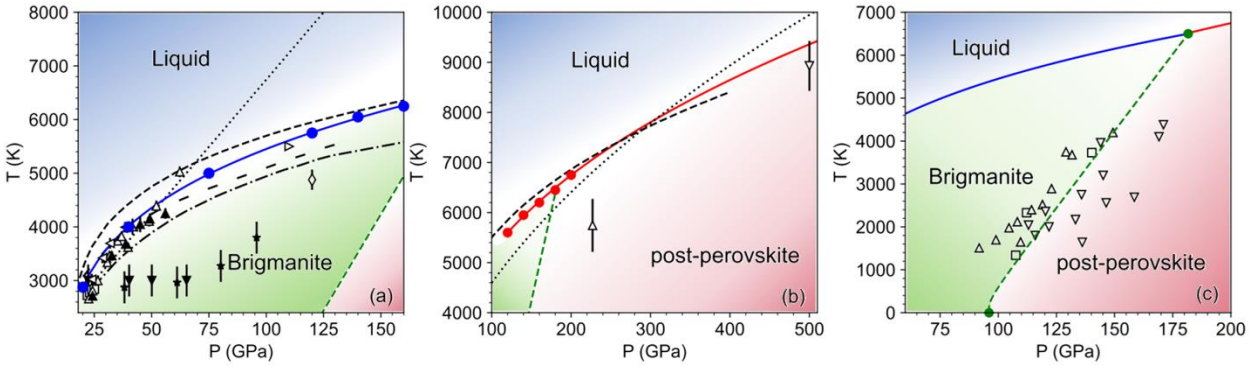

Figure 9. Melting of $MgSiO_3$ bridgmanite **(a)**, post-perovskite **(b)**, and the phase boundary between bridgmanite and post-perovskite **(c)**. Results from this study are shown solid blue circles for bridgmanite, red circles for post-perovskite, green circles for triple point and zero-K transition point. The uncertainties for melting temperatures are 50 K. The solid colored lines in **(a)** and **(b)** represent the Simon fit. The green dashed line in (a), (b), and (c) is the bridgmanite-post-perovskite phase transition boundary. Blue, green, and red shadings cover the stability fields of liquid, bridgmanite, and post-perovskite, respectively. **(a)** Previous experimental results on melting of $MgSiO_3$ bridgmanite are denoted by upward triangles [8], squares [51], leftward triangles [52], rightward triangles [53]. Experimental results of bridgmanite containing ~10 mol% Fe are shown in solid dark upward triangles [8], downward triangles [9], and stars [54]. Prediction based on

Lindemann law is shown dotted line [8]. Estimates based on atomistic modeling includes two-phase simulations based on classical potential with corrections [15] (dashed line), molecular dynamics simulations with empirical overheating correction [16] (loosely dashed line), and [17] (thin diamond), the integration of Clausius-Clapeyron equation by [33] (dashed-dotted line). **(b)** Previous results for the melting of post-perovskite include two shock compression experiments [11] (upward triangle) and [10] (downward triangle), the inferred melting curve using the Lindemann law [4] (dotted line), and two-phase simulations based on classical potential with corrections [15] (dashed line). **(c)** The results of sub-solidus experiments of $MgSiO_3$ [55,56] are shown with upward triangles, downward triangles, and squares denoting bridgmanite-only, post-perovskite-only, and bridgmanite-post-perovskite coexistence, respectively.

Table 1. Calculated melting properties of $MgSiO_3$: pressure P, melting temperatures T_m, slope of the melting curve dT/dP, volume (ΔV_m) and entropy (ΔS_m) of melting at the melting point. Entropy is shown in Nk_B unit where N is the number of atoms per formula unit and k_B is the Boltzmann constant.

Phase	P (GPa)	T_m (K)	dT/dP (K/GPa)	ΔV_m (Å^3/atom)	ΔS_m (Nk_B)
Bridgmanite	20	2875(50)	95.1(4.7)	1.26(0.02)	0.95(0.04)
	40	4000(50)	38.3(1.2)	0.71(0.01)	1.33(0.04)
	75	5000(50)	21.2(0.6)	0.43(0.02)	1.46(0.04)
	120	5750(50)	14.3(0.5)	0.27(0.02)	1.38(0.04)
	140	6050(50)	12.6(0.4)	0.21(0.02)	1.20(0.04)
	160	6250(50)	11.4(0.4)	017(0.01)	1.11(0.04)
Post-perovskite	120	5600(50)	17.2(3.1)	0.35(0.01)	1.49(0.27)
	140	5950(50)	15.5(2.7)	0.31(0.01)	1.45(0.25)
	160	6200(50)	14.2(2.5)	0.27(0.02)	1.41(0.24)
	180	6450(50)	13.1(2.2)	0.25(0.02)	1.37(0.23)
	200	6750(50)	12.2(2.1)	0.23(0.02)	1.33(0.23)

Our results agree well with a number of experimental studies at the low-pressure end of the bridgmanite stability field (Fig. 9). In order to better constrain the slope of the bridgmanite melting curve, we have performed a simulation at 20 GPa, below the stability field of bridgmanite, but accessible to our simulations because of kinetic hindrances to crystal-crystal transitions. At 20 GPa, we obtained a melting temperature of 2875±50 K, slightly higher than the result (i.e., 2700±50 K) of the multi-anvil experiments [51], suggesting that PBEsol may overestimate the melting temperature consistent with the previous study on MgO melting [46]. Our melting curve of $MgSiO_3$ bridgmanite may be expressed by the Simon equation, $T_m = 2875 \pm 50\left(\frac{P-20}{8.11\pm0.37}+1\right)^{\frac{1}{3.73\pm0.06}}$, where T_m is in K and P in GPa. This fitted melting curve agrees very well with the results of some laser-heated diamond anvil cell experiments [8,52] up to 50 GPa. The resulting melting slope at 25 GPa is around 69 K/GPa, broadly consistent with experimental result of ~80 K/GPa by ref. [8], but deviate from the results of ref. [9,54] (~0 K/GPa), and those of ref. [51] (30

K/GPa), implying a vanishing small volume of melting, contrary to our findings and that of previous *ab initio* determination of the volume of melting [33]. Our results agree well with the only determination of the melting temperature at pressure greater than 100 GPa from shock wave experiments [53].

The melting temperature of post-perovskite increases more rapidly with increasing pressure than that of bridgmanite (Fig. 9b); our results can be represented by $T_m = 5600 \pm 50\left(\frac{P-120}{113.60\pm16.13}+1\right)^{\frac{1}{2.85\pm0.32}}$. Our melting curve is consistent with a shock wave measurement of melting at 500 GPa [10], but is significantly higher than that determined in another study at 210 GPa [11]. We note that extrapolating the melting curve beyond ~200 GPa is subject to uncertainty: for example, our best-fit melting curve of post-perovskite predicts a melting point of 9376±656 K at 500 GPa. More experiments at these extreme conditions are clearly warranted.

From our simulations, we also determine the volume of melting, and from the Clausius-Clapeyron relation, the entropy of melting (Table 1, Fig. 10). The volume of melting diminishes rapidly with increasing pressure because the liquid is more compressible than the solid. The entropy of melting initially increases with increasing pressure and then decreases with increasing pressure at pressure greater than 100 GPa. The volume and entropy of melting increase at the triple point as the volume and entropy of the post-perovskite are less than those of the bridgmanite phase.

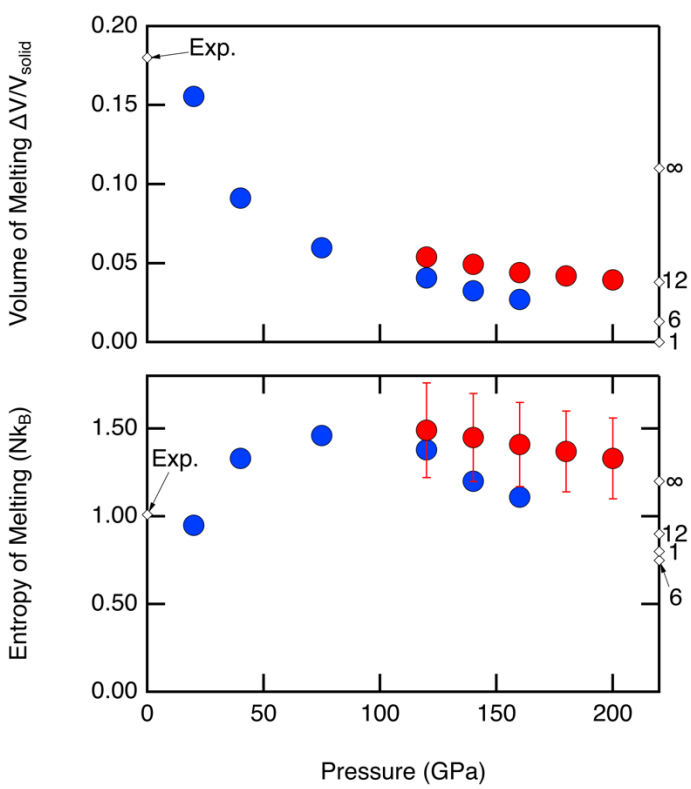

Figure 10. The volume (top) and the entropy (bottom) of melting from the bridgmanite (blue) and the post-perovskite (red) phases. For comparison we also show experimental values for

melting from the low-pressure enstatite structure [57,58], and theoretical results for the melting of monatomic systems interacting with inverse-power repulsion with the value of the power indicated ranging from 1 (one-component plasma) to infinite (hard-spheres)[59].

D. Bridgmanite to post-perovskite transition

The intersection of the melting curves of bridgmanite and post-perovskite yields the bridgmanite/post-perovskite/liquid triple point at 180 GPa and 6420 K (Fig. 9). We combine this result with our computed values for the phase transition pressure at 0 K (96 GPa), the volume contrast between the two phases (0.467 $Å^3$/formula unit) and the Einstein temperatures of the two phases (773 K for bridgmanite and 791 K for post-perovskite) to determine the solid-solid phase boundary following the formalism of Jeanloz (1989) which accounts for the vanishing Clapeyron slope in the limit of zero temperature (Fig. 9c). The resulting Clapeyron slope at 2000 K is 13.9 MPa/K, very close to the experimental result of 13.3±1.0 MPa/K [55], although we note that the experimental value may have considerable systematic uncertainty due to the non-unique choice of pressure scale [14].

IV. DISCUSSION

A. Melting Curve and Crystal Buoyancy

The Lindemann law has been widely used to predict the melting curve of materials including at high pressure [60,61]. We find that for both bridgmanite and post-perovskite, the Lindemann law tends to predict much larger melting slopes (dT_m/dP), thus leading to extremely high melting temperatures at high pressure (Fig. 9). The difference between our results and the Lindeman law reveals the importance of liquid structure. Whereas the Lindemann law can be derived by assuming that scaled liquid structure is constant along the melting curve. We find, in agreement with previous studies, that liquid structure changes substantially with increasing pressure [33]. Moreover, the change in the liquid strucutre, including increases in the Si-O coordination number, are such as to cause the liquid to become denser with increasing pressure, thus decreasing the volume of melting and the Clapeyron slope.

The entropy of melting determined here (Table 1, Fig. 10) is much larger than that of many monatomic systems at high pressure (Rln2 where R is the gas constant) [62]. We attribute the larger entropy of melting to the range of different Si-O coordination environments in the liquid present at all pressures, producing a liquid structure that is much richer than the nearly close-packed structures of monatomic liquids. At the highest pressures of our simulations, the entropy of melting decreases with increasing pressure, but is still much larger than Rln2, and larger than that of simple monatomic liquids interacting with inverse-power repulsion.

The volume of the liquid closely approaches, but does not fall below that of the solid phases (Table 1, Fig. 10). The volume of melting at the highest pressure of our study (4 %) is much less than that at ambient pressure (18 %), reflecting the greater compressibility of the liquid as compared

with solid phases. The very small volume of melting that we find means that crystals freezing out of deep molten portions of rocky planets, are likely to be buoyant. With similar volumes, the liquid is likely to be denser than coexisting crystals because major heavy elements, like Fe, tend to partition favorably into the liquid. Deep crystal buoyancy in cooling rocky planets has important implications for understanding their thermal and chemical evolution [7,63].

B. Thermal structure of Earth's lowermost mantle

To examine whether the bridgmanite to post-perovskite transition may be encountered in the deep Earth, we assume that the geotherm consists of an adiabat and a lower thermal boundary layer, following previous studies [13]

$$T(r) = T_{CMB} - (r - r_{CMB})T_S' - \Delta T \mathrm{erf}\left(\frac{r - r_{CMB}}{\delta}\right) \qquad (12)$$

where $T(r)$ is the temperature as a function of radius, subscript *CMB* indicates values at the core-mantle boundary, ΔT and δ are the temperature contrast and thickness of the thermal boundary layer, respectively, and T_S' is the adiabatic gradient at the base of the mantle. The pressure of the CMB is 136 GPa and temperature (T_{CMB}) is assumed to be 4000 K. We compute the adiabat $T_S(r)$ for a given potential temperature from HeFESTo [64-66], yielding the adiabatic gradient T_S' and the temperature contrast $\Delta T = T_{CMB} - T_S(r_{CMB})$. The heat flux at the core-mantle boundary is then

$$F_{CMB} = k\left(T_S' + \frac{2}{\sqrt{\pi}}\frac{\Delta T}{\delta}\right) \qquad (13)$$

with the thermal conductivity k=8.1 W/m/K[67].

Our results for the bridgmanite to post-perovskite phase transition suggests that post-perovskite may exist as a lens in the cooler parts of the deep lower mantle (Fig. 9). Along an average mantle geotherm with the potential temperature T_P=1600 K and a bottom thermal boundary layer of greater than δ=120 km thickness, only bridgmanite is stable and post-perovskite is absent, consistent with the absence of observations of seismic reflections from the lowermost mantle in most regions [68]. If we examine a geotherm representative of a cooler portion of the mantle (T_P =1300 K, d=170 km), we find two crossings of the bridgmanite to post-perovskite transition, at 100 and 300 km above the core-mantle boundary. The depths to these reflections are consistent with paired reflections of opposite polarity seen in cooler parts of the mantle [13,69]. The presence of a post-perovskite lens therefore places important constraints on the thermal structure of the lower-most mantle and on the heat flow emanating from the core. For our cool model geotherm, we find a heat flux into the base of the mantle of 100 mW/m^2, or 15 TW. This heat flux is more than sufficient to drive dynamo action in the underlying outer core [70]. In detail, the pressure-temperature conditions of the bridgmanite to post-perovskite transition may depend on the concentration of Fe, Al, and other secondary oxides [71]. Moreover, the heat flux into the mantle is likely to vary greatly laterally, and may approach zero in some regions of the mantle [67]. Our result for the cool mantle geotherm is therefore consistent with a global average heat flux of

80 mW/m^2 or 12 TW, which agrees with estimates of the minimum heat flux required to drive magnetic field generation in the underlying core.

V. Conclusion

It is now possible to develop machine learning potentials that accurately capture the physics of multiple phases in multi-atom systems over a wide range of pressure and temperature. We have overcome the challenges posed by planetary-scale applications with an iterative training scheme that entails multithermal-multibaric enhanced sampling driven by structure factors as collective variables, feature selection, deep learning, and DFT calculations. This scheme allows us to build a MLP of $MgSiO_3$ liquid, bridgmanite, and post-perovskite up to 220 GPa and 8000 K using only 4324 training frames. The phase stability relations that we have determined using this machine learning potential place important constraints on processes in the deep Earth and in super-Earth exoplanets. Liquids are likely to be denser than coexisting solids within the bridgmanite and post-perovskite pressure-ranges of stability. The Clapeyron slope of the bridgmanite to post-perovskite transition indicates the presence of double-crossings of the phase transition in colder portions of the mantle, consistent with seismic observations and heat flux from the core-mantle boundary compatible with magnetic field generation in Earth's outer core.

Data Availability

The main data supporting the findings of this study are available within the paper and its supplementary information. Data set used in this study has been deposited at the Open Science Framework (https://osf.io/dt4xs/) with doi: 10.17605/OSF.IO/DT4XS. The software packages used in this study are standard codes: VASP (version 5.4) is a commercial code (see www.vasp.at) whereas DeePMD-kit (https://github.com/deepmodeling/deepmd-kit), PHONOPY (http://phonopy.github.io/phonopy/), LAMMPS (https://www.lammps.org/), PLUMED 2 (https://www.plumed.org/doc-v2.6/user-doc/html/index.html), HeFESTo (https://github.com/stixrude/HeFESToRepository) and ASAP (https://github.com/BingqingCheng/ASAP) are open-source.

ACKNOWLEDGMENTS

We thank Ian Ocampo for helpful discussions. We are grateful to reviewers for comments that improved the manuscript. We acknowledge the following grants: National Science Foundation (EAR-1853388 to Lars Stixrude), National Natural Science Foundation of China (grant No. 22003050 to Haiyang Niu), and the Research Fund of the State Key Laboratory of Solidification Processing (NPU), China (grant No. 2020-QZ-03 to Haiyang Niu). This work used computational and storage services associated with the Hoffman2 Shared Cluster provided by UCLA Institute for Digital Research and Education's Research Technology Group.

References

[1] C. Dorn, A. Khan, K. Heng, J. A. D. Connolly, Y. Alibert, W. Benz, and P. Tackley, A&A **577**, A83 (2015).

[2] B. J. Fulton and E. A. Petigura, The Astronomical Journal **156**, 264 (2018).

[3] C. Dorn and T. Lichtenberg, The Astrophysical Journal Letters **922**, L4 (2021).

[4] L. Stixrude, Philos Trans A Math Phys Eng Sci **372**, 20130076 (2014).

[5] R. G. Kraus, R. J. Hemley, S. J. Ali, J. L. Belof, L. X. Benedict, J. Bernier, D. Braun, R. E. Cohen, G. W. Collins, F. Coppari *et al.*, Science **375**, 202 (2022).

[6] A. Boujibar, P. Driscoll, and Y. Fei, Journal of Geophysical Research: Planets **125**, e2019JE006124 (2020).

[7] S. Labrosse, J. W. Hernlund, and N. Coltice, Nature **450**, 866 (2007).

[8] A. Zerr and R. Boehler, Science **262**, 553 (1993).

[9] D. L. Heinz and R. Jeanloz, Journal of Geophysical Research: Solid Earth **92**, 11437 (1987).

[10] Y. Fei, C. T. Seagle, J. P. Townsend, C. A. McCoy, A. Boujibar, P. Driscoll, L. Shulenburger, and M. D. Furnish, Nature Communications **12**, 876 (2021).

[11] D. Fratanduono, M. Millot, R. G. Kraus, D. K. Spaulding, G. W. Collins, P. M. Celliers, and J. H. Eggert, Phys Rev B **97**, 214105 (2018).

[12] K. Umemoto, R. M. Wentzcovitch, S. Wu, M. Ji, C.-Z. Wang, and K.-M. Ho, Earth and Planetary Science Letters **478**, 40 (2017).

[13] T. Lay, J. Hernlund, E. J. Garnero, and M. S. Thorne, Science **314**, 1272 (2006).

[14] S.-H. Shim, Annual Review of Earth and Planetary Sciences **36**, 569 (2008).

[15] A. B. Belonoshko, N. V. Skorodumova, A. Rosengren, R. Ahuja, B. Johansson, L. Burakovsky, and D. L. Preston, Phys Rev Lett **94**, 195701 (2005).

[16] Z.-J. Liu, C.-R. Zhang, X.-W. Sun, J.-B. Hu, T. Song, and Y.-D. Chu, Physica Scripta **83**, 045602 (2011).

[17] C. Di Paola and J. P. Brodholt, Scientific Reports **6**, 29830 (2016).

[18] D. Alfè, M. J. Gillan, and G. D. Price, The Journal of Chemical Physics **116**, 6170 (2002).

[19] D. Alfè, Phys Rev Lett **94**, 235701 (2005).

[20] L. Vočadlo, D. Alfè, G. D. Price, and M. J. Gillan, The Journal of Chemical Physics **120**, 2872 (2004).

[21] J. Behler and M. Parrinello, Phys Rev Lett **98**, 146401 (2007).

[22] L. Zhang, J. Han, H. Wang, R. Car, and W. E, Phys Rev Lett **120**, 143001 (2018).

[23] M. Yang, T. Karmakar, and M. Parrinello, Phys Rev Lett **127**, 080603 (2021).

[24] P. M. Piaggi and M. Parrinello, Phys Rev Lett **122**, 050601 (2019).

[25] H. Niu, L. Bonati, P. M. Piaggi, and M. Parrinello, Nature Communications **11**, 2654 (2020).

[26] G. A. Tribello, M. Bonomi, D. Branduardi, C. Camilloni, and G. Bussi, Computer Physics Communications **185**, 604 (2014).

[27] S. Plimpton, Journal of Computational Physics **117**, 1 (1995).

[28] H. Wang, L. Zhang, J. Han, and W. E, Computer Physics Communications **228**, 178 (2018).

[29] H. Niu, P. M. Piaggi, M. Invernizzi, and M. Parrinello, Proceedings of the National Academy of Sciences **115**, 5348 (2018).

[30] H. Niu, Y. I. Yang, and M. Parrinello, Phys Rev Lett **122**, 245501 (2019).

[31] P. M. Piaggi and M. Parrinello, The Journal of Chemical Physics **150**, 244119 (2019).

[32] J. Deng and L. Stixrude, Geophysical Research Letters **562**, 116873 (2021).

[33] L. Stixrude and B. Karki, Science **310**, 297 (2005).

[34] A. P. Bartók, R. Kondor, and G. Csányi, Phys Rev B **87**, 184115 (2013).

[35] G. Imbalzano, A. Anelli, D. Giofré, S. Klees, J. Behler, and M. Ceriotti, The Journal of Chemical Physics **148**, 241730 (2018).

[36] B. Cheng, R.-R. Griffiths, S. Wengert, C. Kunkel, T. Stenczel, B. Zhu, V. L. Deringer, N. Bernstein, J. T. Margraf, K. Reuter *et al.*, Accounts of Chemical Research **53**, 1981 (2020).
[37] H. Wang, L. Zhang, J. Han, and E. Weinan, Comput. Phys. Commun. **228**, 178 (2018).
[38] S. Lorenz, A. Groß, and M. Scheffler, Chemical Physics Letters **395**, 210 (2004).
[39] K. Hornik, M. Stinchcombe, and H. White, Neural Networks **2**, 359 (1989).
[40] J. P. Perdew, A. Ruzsinszky, G. I. Csonka, O. A. Vydrov, G. E. Scuseria, L. A. Constantin, X. Zhou, and K. Burke, Phys Rev Lett **100**, 136406 (2008).
[41] G. Kresse and J. Furthmüller, Computational Materials Science **6**, 15 (1996).
[42] G. Kresse and D. Joubert, Phys Rev B **59**, 1758 (1999).
[43] E. Holmström and L. Stixrude, Phys Rev Lett **114**, 117202 (2015).
[44] R. Scipioni, L. Stixrude, and M. P. Desjarlais, Proceedings of the National Academy of Sciences **114**, 9009 (2017).
[45] J. Deng and L. Stixrude, Earth and Planetary Science Letters **562**, 116873 (2021).
[46] Y. Yoshimoto, Journal of the Physical Society of Japan **79**, 034602 (2010).
[47] W. G. Hoover, Phys Rev A **31**, 1695 (1985).
[48] N. D. Mermin, Physical Review **137**, A1441 (1965).
[49] A. Togo and I. Tanaka, Scripta Materialia **108**, 1 (2015).
[50] S. Baroni, S. de Gironcoli, A. Dal Corso, and P. Giannozzi, Rev Mod Phys **73**, 515 (2001).
[51] E. Ito and T. Katsura, in *High‐Pressure Research: Application to Earth and Planetary Sciences*1992), pp. 315.
[52] G. Shen and P. Lazor, Journal of Geophysical Research: Solid Earth **100**, 17699 (1995).
[53] J. A. Akins, S.-N. Luo, P. D. Asimow, and T. J. Ahrens, Geophysical Research Letters **31** (2004).
[54] E. Knittle and R. Jeanloz, Geophysical Research Letters **16**, 421 (1989).
[55] S. Tateno, K. Hirose, N. Sata, and Y. Ohishi, Earth and Planetary Science Letters **277**, 130 (2009).
[56] K. Hirose, R. Sinmyo, N. Sata, and Y. Ohishi, Geophysical Research Letters **33** (2006).
[57] R. A. Lange and I. S. E. Carmichael, Geochimica et Cosmochimica Acta **51**, 2931 (1987).
[58] J. F. Stebbins, I. S. E. Carmichael, and L. K. Moret, Contributions to Mineralogy and Petrology **86**, 131 (1984).
[59] D. A. Young, *Phase diagrams of the elements* (University of California Press, Berkeley, 1991).
[60] J. Deng and K. K. M. Lee, Am Mineral **104**, 1189 (2019).
[61] G. H. Wolf and R. Jeanloz, Journal of Geophysical Research: Solid Earth **89**, 7821 (1984).
[62] S. M. Stishov, I. N. Makarenko, V. A. Ivanov, and A. M. Nikolaenko, Physics Letters A **45**, 18 (1973).
[63] L. Stixrude, N. de Koker, N. Sun, M. Mookherjee, and B. B. Karki, Earth and Planetary Science Letters **278**, 226 (2009).
[64] L. Stixrude and C. Lithgow-Bertelloni, Geophys J Int **162**, 610 (2005).
[65] L. Stixrude and C. Lithgow-Bertelloni, Geophys J Int **184**, 1180 (2011).
[66] L. Stixrude and C. Lithgow-Bertelloni, Geophys J Int **228**, 1119 (2021).
[67] S. Stackhouse, L. Stixrude, and B. B. Karki, Earth and Planetary Science Letters **427**, 11 (2015).
[68] L. Cobden, C. Thomas, and J. Trampert, in *The Earth's Heterogeneous Mantle: A Geophysical, Geodynamical, and Geochemical Perspective*, edited by A. Khan, and F. Deschamps (Springer International Publishing, Cham, 2015), pp. 391.
[69] C. Thomas, E. J. Garnero, and T. Lay, Journal of Geophysical Research: Solid Earth **109** (2004).
[70] F. Nimmo, in *Treatise on Geophysics (Second Edition)*, edited by G. Schubert (Elsevier, Oxford, 2015), pp. 27.
[71] B. Grocholski, K. Catalli, S.-H. Shim, and V. Prakapenka, Proceedings of the National Academy of Sciences **109**, 2275 (2012).